



Article

Analysis of Optimal Loading Angle in Dynamic Flattened Brazilian Disc Splitting Test for Concrete

Benjun Shi ¹, Haozhe Xing ^{1,*}, Chaomin Mu ^{2,*}, Jie Li ¹, Tianhan Xu ¹  and Wei Liu ³ 

¹ State Key Laboratory of Explosion & Impact and Disaster Prevention & Mitigation, Army Engineering University of PLA, Nanjing 210007, China

² School of Safety Science and Engineering, Anhui University of Science and Technology, Huainan 232001, China

³ Institute of Engineering Safety and Disaster Prevention, Hohai University, Nanjing 210098, China

* Correspondence: haozhexing@hotmail.com (H.X.); 200204030003@hhu.edu.cn (C.M.)

Abstract: The mechanism of crack expansion in conventional Brazilian discs is clearly obtained with the help of numerical simulations, and the direction of crack expansion is related to the loading speed. Then the relationship between the stress field and the platform angle was given quantitatively based on the theoretical analysis. To obtain the accurate tensile strength of self-compacting concrete under the premise of numerical simulation and theoretical analysis, flattened Brazilian disc (BD) splitting tests with six loading angles were carried out by using the split Hopkinson pressure bar (SHPB) loading system. The crack initiation mode and fracture propagation mode of specimens under different loading angles and loading rates were analyzed through digital image correlation (DIC) and strain gauges. When the loading angle lies between 28° and 30°, the specimens easily meet the requirement of central cracking under high loading rates. The experimental results were well explained with theoretical analysis from a view of dimensionless Griffith's equivalent stress. The dynamic tensile strength measured from the non-central crack mode in flattened BD splitting tests underestimates the inherent dynamic tensile strength.

Keywords: self-compacting concrete; dynamic tensile strength; flattened Brazilian disc test; optimal loading angle; digital image correlation; numerical simulation



Citation: Shi, B.; Xing, H.; Mu, C.; Li, J.; Xu, T.; Liu, W. Analysis of Optimal Loading Angle in Dynamic Flattened Brazilian Disc Splitting Test for Concrete. *Appl. Sci.* **2022**, *12*, 11834. <https://doi.org/10.3390/app122211834>

Academic Editor: Dario De Domenico

Received: 2 November 2022

Accepted: 16 November 2022

Published: 21 November 2022

Publisher's Note: MDPI stays neutral with regard to jurisdictional claims in published maps and institutional affiliations.



Copyright: © 2022 by the authors. Licensee MDPI, Basel, Switzerland. This article is an open access article distributed under the terms and conditions of the Creative Commons Attribution (CC BY) license (<https://creativecommons.org/licenses/by/4.0/>).

1. Introduction

Currently, explosions are common across the globe, posing a serious threat to human life and causing dramatic damage to homes and infrastructure. The latter has received attention from scholars in the field of structural engineering who study the effects of blast and impact on different RC members (beams, columns, slabs, silos, etc.) [1–4].

When a pressure pulse is reflected as a tensile pulse in a column or on the free surface of a slab, it will likely cause a fairly high tensile stress somewhere adjacent to the free surface, and once a certain dynamic fracture criterion is met, it will cause the tensile rupture of the material at that location. When the crack is large enough, the whole lobe flies away with the momentum caught in it. This dynamic tensile fracture on the back side caused by the reflection of pressure pulses on the free surface is called spalling. The lobes that fly out are called scab. In the above case, once a lamellar crack appears, a new free surface is also formed at the same time. Continued incident pressure pulses are then reflected on this new free surface, which may cause a second spalling of lamination cracks. By analogy, a series of multi-layer lamellar fractures can be formed under certain conditions to produce a series of multi-spalling lamellar fractures. Therefore, it is of great importance to obtain the accurate tensile strength of concrete materials for the safe design of civil engineering structures [5–7].

Testing methods to determine the tensile strength of brittle materials can be divided into direct tensile methods [8–10] and indirect tensile methods [11–15]. The direct tensile

method obtains the tensile strength of concrete in a straightforward manner, but the difficulty in achieving a uniaxial tensile stress state and the irregularity of the experimental operation may lead to local stress concentration and cause a non-standard damage pattern. On the other hand, indirect tensile testing methods, such as the Brazilian disc (BD) test [16], Ring method [17], and the Luong method [18], have received extensive attention due to their feasibility and simplicity of operation. Among them, the BD test has been adopted as the suggested testing method by the ISRM [19] and ISO standards [20] for testing the tensile strength of rock materials, and it has been designated as the standard method in ASTM C496 and DIN EN 12390-6 for testing the tensile strength of concrete materials [21,22].

However, previous research [23–26] has pointed out that nonnegligible stress concentration can easily be generated at the interface between BD specimen and loading platen, which results in cracks forming at the loading edge rather than the center of the specimen. The crack initiation at the loading edge does not satisfy the Griffith strength criterion, bringing out unreliable tensile strength. Therefore, efforts have been made to improve the loading configuration of BD splitting experiments to ensure the validity of the results.

The improvement to reduce the stress concentration basically falls into two categories: the arc-loaded BD test and the flattened BD test. In terms of the arc-loaded BD test, Hondros et al. [27] gave theoretical solutions of the whole stress and displacement fields for the specimen under radial loading on a finite arc, which turned out to be superior to the original concentrated load. However, in-depth error analysis is absent for the approximate expressions describing the relevant stress components, and it is difficult to achieve the required uniform radial loads distributed over a pair of circular arcs in practical experiments [28,29]. Regarding the flattened BD test, the loading angle greatly affects the validity of the results. With the help of the finite element method, it was found that to ensure the central cracking of the sample, the loading angle should be no less than 19.5° [30,31]. Meanwhile, Wang et al. [32,33] found that if the loading angle was too large, the failure of the specimen tended to deviate from the symmetry plane. Based on cusp catastrophe theory, he suggested that the loading angle should be no larger than 30° . Kaklis et al. [34] proposed two loading modes for the flattened BD tests: (1) uniformly distributed loads directly act on the specimen and (2) loads indirectly act on the specimen through a cushion block. It was concluded that the loading angle must be no less than 20° for the first loading mode, while in the second loading mode, the loading angle must be no less than 15° . The recommended loading angles are basically between 15° and 30° for rock materials tests, while little research was reported on concrete materials. Whether those conclusions obtained from rocks can be extended to concrete at a high loading rate remains unknown.

The purpose of this study is to explore the influence of the loading angle on the failure of self-compacting concrete (SCC) and subsequently determine the optimal range of the loading angle to measure the tensile strength of SCC in the flattened BD test under dynamic load. Initially, the numerical simulation of the traditional Brazilian disc was carried out to study the mechanism of crack propagation. Secondly, the theoretical analysis of the platform Brazilian disc was carried out to study the influence of different loading angles on the stress field. Finally, the flattened Brazilian splitting experiment was implemented with a split Hopkinson pressure bar (SHPB). The crack initiation and failure process were detected by both digital image correlation (DIC) and strain gage. The relationship between loading angle and dynamic tensile strength of SCC was obtained.

2. Numerical Simulations

The mechanics of Brazilian splitting of disc self-compacting concrete under dynamic loads is first investigated by means of numerical simulations. The set speeds of the projectile with a length of 400 mm are 4.9 m/s, 9.6 m/s, and 12.5 m/s, respectively, where the projectile was defined as kinetic energy penetrators, and the impact compression of the disc concrete specimen is obtained to obtain the whole process of dynamic fracture evolution.

The numerical simulation of Brazilian splitting uses a plane strain assumption, the diameter of the numerical specimen is 50 mm, the model mesh adopts a mapping mesh,

the element size is 0.25 mm, and the whole model contains a total of 10,000 cells and 10,201 nodes. The loading process is controlled by speed, and the boundary conditions are deformation in the z-direction of the fixed model, the speed boundary condition in the x direction of the projectile is applied to the model, and the transmission rod is fixed and constrained.

A total of 61 measuring points are arranged along the central profile of the length of the Brazilian splitting disc specimen, and the spacing between each measuring point is 5 mm, of which the No. 6 measurement point is arranged in the center of the circle, as shown in Figure 1. Using the JHC (Johnson Holmquist Concrete) constitutive model [35,36], the numerical model parameters are shown in Table 1. When the model element is yielded, the cohesion and tensile strength of the unit gradually soften linearly with the accumulation of plastic shear strain and plastic tensile strain. When the plastic shear strain and plastic tensile strain accumulate to the critical value, the cohesion and tensile strength of the unit weaken to the residual strength and remain unchanged.

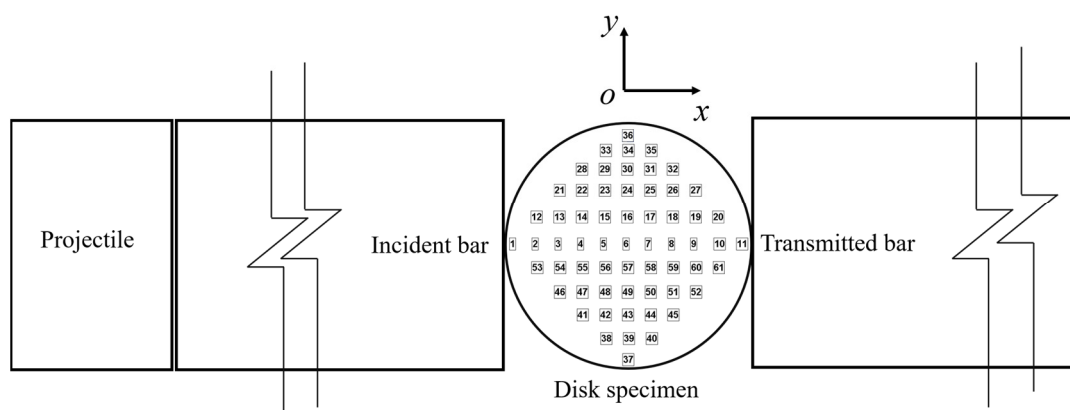


Figure 1. Schematic diagram of Brazilian cleavage (The numbers in the figure indicate the monitoring points).

Table 1. Material parameters of JHC model.

Sign	$\rho/\text{kg}\cdot\text{m}^{-3}$	f_c/MPa	G/GPa	A	B	C	N	T/MPa	ϵ_{fmin}
Value	2425	52	13.9	0.80	1.60	0.007	0.61	3	0.007
Sign	P_c/MPa	μ_c	P_1/MPa	μ_1	D_1	D_2	K_1/MPa	K_2/MPa	K_3/MPa
Value	11.7	6.26×10^{-4}	800	0.06	0.0452	10	85	-171	208

In the plane of the Brazilian disc, any pair of symmetry points, as shown in Figure 2, the compressive stress on the symmetry point are symmetrical, indicating that the specimen can be maintained in a dynamic force equilibrium state during the dynamic load process.

As shown in Figure 3(a₀)–(c₀), at a velocity of 4.9 m/s, the stress wave first forms a compression crack at the end of the incident rod due to the dynamic load. From Figure 4a, it can be seen that the compressive stress peak at 32.08 μs formed a compressive stress of 205.6 MPa at measurement point 1, and then the compressive stress decayed rapidly. As the tensile stress increases along the radial loading direction, as shown in Figure 4d, before $t = 40 \mu\text{s}$, the tensile stress is small, and the mean tensile stress is about 2.5 MPa, which is not enough to produce damage. In $t = 50\text{--}80 \mu\text{s}$, the tensile stress from measurement point 3 to measurement point 9 is generally increased, and the average value is about 7.5 MPa. At $t = 50 \mu\text{s}$, the compressive stress propagates to the transmission bar end and begins to reflect, and the incident wave and the reflected wave are the same sign, showing the loading process.

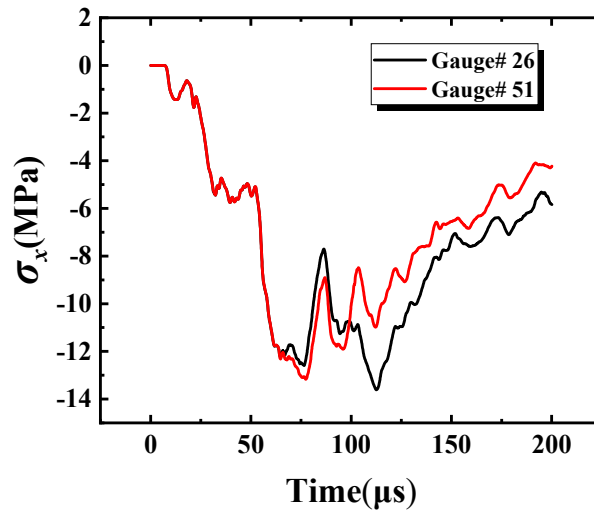


Figure 2. Symmetrical measurement point stress change of disc specimens.

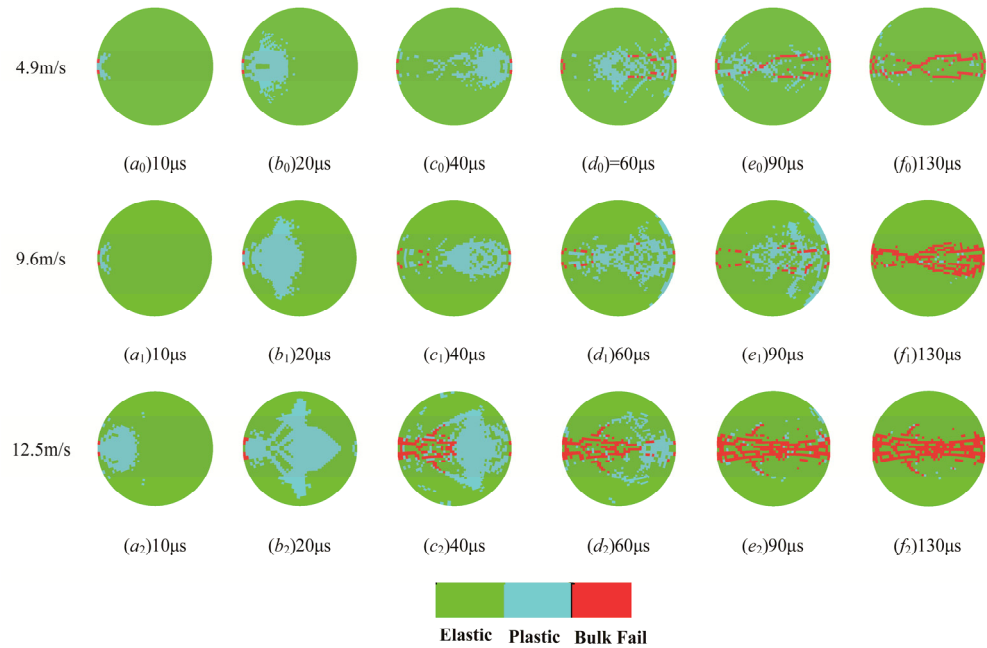


Figure 3. Crack evolution of disc specimens under dynamic load.

From Figure 4a, it can be seen that the reflected compressive stress peak at 55.71 μs at the measuring point 11 forms a compressive stress of 212.06 MPa, which is 1.031 times the compressive stress of measurement point 1, which plays a guiding role in the direction of crack propagation; that is, the crack begins to expand from the transmission bar end along the loading diameter direction, and the action of the incident bar is until it extends to the end of the incident bar end, as detailed in Figure 3(d₀)–(f₀). As shown in Figure 3(a₁), (b₁), there is a similar phenomenon at a speed of 9.6 m/s and at the previous speed of 4.9 m/s, but the peak compressive stress is higher than the previous one.

From Figure 4b, it can be seen that the compressive stress peak at 22.08 μs formed a compressive stress of 286.96 MPa at measurement point 1, and the compressive stress then attenuated equally rapidly. As the pressure stress decays and the tensile stresses increase along the diameter direction of the applied load, as shown in Figure 4e. Before $t = 40 \mu\text{s}$, the tensile stress of measuring points 3, 4 and 5 is close to the tensile stress of measurement point 1 and the tensile stress average is 8.5 MPa, since the tensile stress wave is felt before

measuring point 6, so under dynamic load, it is not the center of the circle that first begins to crack but the tensile crack occurs at the middle of the incident rod end and the center of the circle, as shown in Figure 3(c₁).

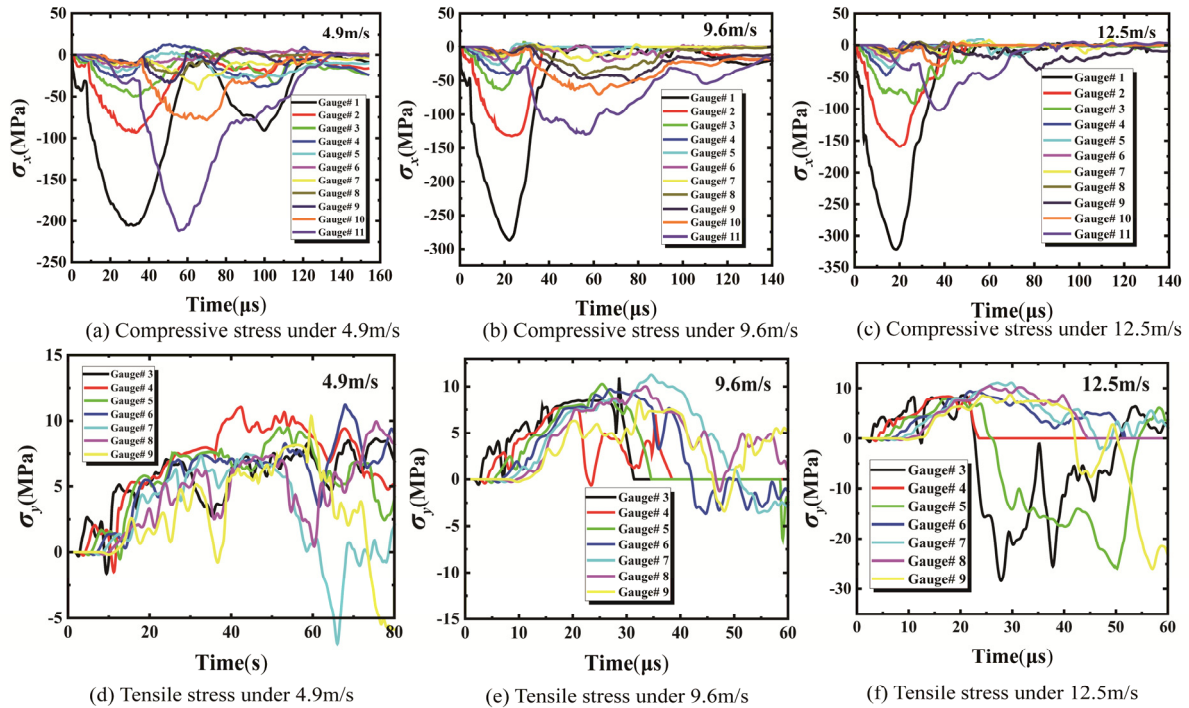


Figure 4. Measurement point compression and tensile stress distribution in the radial loading direction.

From Figure 4b, it can be seen that at $t = 57 \mu s$, the compressive stress propagation to the transmission bar end begins to reflect, and the peak of the reflected compressive stress decreases to 130 MPa, which is caused by the increase in the projectile speed and the increase in the crack in the test piece. Under the action of reflected compressive stress, there are tensile cracks at the transmission end and center of the circle, and finally the previous crack converges to form a main crack, as shown in Figure 3(d₁)–(f₁).

When the velocity increases to 12.5 m/s, the crack formation is consistent with the law of 9.6 m/s at a velocity, but the tensile stress strength increases, the number of cracks increases, and the crack propagation mechanism is consistent. There is no repetition here. Through numerical simulation, it was found that there was a problem of non-central cracking of traditional Brazilian discs, and then the platform angle was introduced experimentally to explore this.

3. Theoretical Analysis

It is known from the literature [37] that under the same loading rate the stress at any point in the BD specimen on the loading under the action of horizontal radial concentrated force can be expressed as Appendix A, as shown in Figure 5.

The horizontal stress σ_x in the loading BD specimen decreases from the A_1 and the A_2 to the O , as shown in Figure 6. Moreover, with the increase in the loading angle, the vertical compressive stress decreases significantly, from 18.11 when the loading angle is 20° to 12.21 when the loading angle is 30° , so its change rate with the loading angle is 0.59. The compression–tension stress ratio in the loading BD decreases with the increase in loading angle, as shown in Table 2.

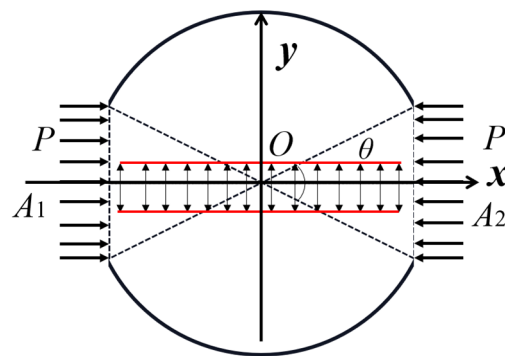


Figure 5. The flattened Brazilian test.

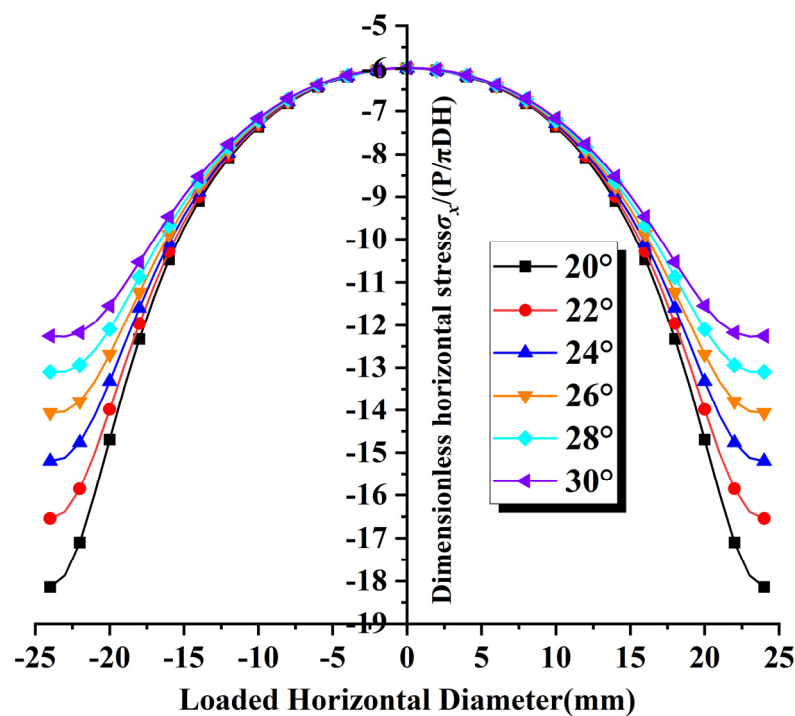


Figure 6. Non-dimensional horizontal stresses along loaded diameter.

Table 2. Ratios of non-dimensional compressive stress to tensile stress inside discs.

Loading Angle (°)	Compressive Stress σ_{xmax}	Compressive Stress σ_{ymax}	Tensile Stress σ_{x1max}	$\sigma_{xmax}/\sigma_{x2max}$	$\sigma_{ymax}/\sigma_{x1max}$
20	18.11	12.87	1.88	9.63	6.84
22	16.52	12.13	1.86	8.88	6.52
24	15.15	11.48	1.83	8.27	6.27
26	13.96	10.90	1.81	7.71	6.02
28	13.08	10.36	1.78	7.34	5.82
30	12.21	9.86	1.74	7.01	5.66

It can be seen from Figure 7 that the maximum value of vertical tensile stress σ_y appears at the O point of the disc and gradually decreases from the O point to both ends A1 and A2 and finally becomes vertical compressive stress. Moreover, with the increase in loading angle, the vertical tensile stress in the BD specimen of the loading decreases slowly, from 1.88 at 20° to 1.74 at 30°, and its change rate with loading angle is 0.014, which can be considered as a constant value. The maximum value of vertical compressive stress is reduced from 12.87 to 9.86.

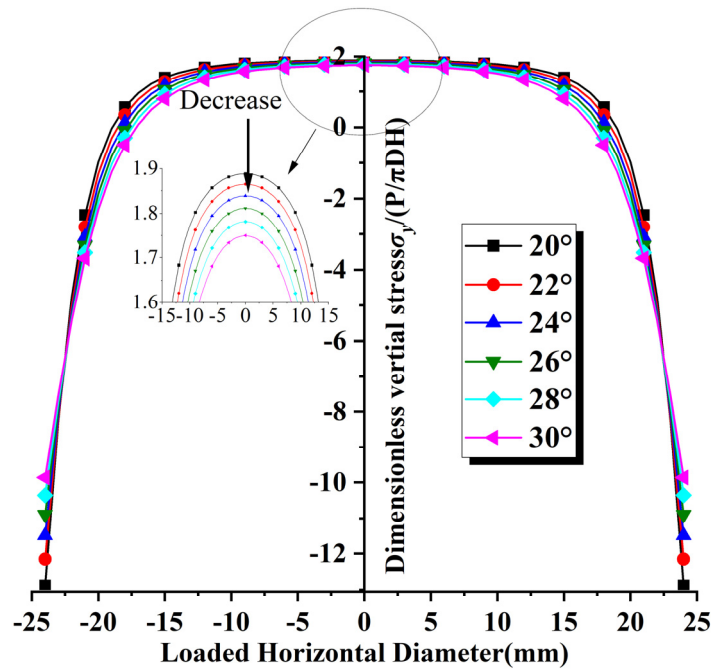


Figure 7. Non-dimensional vertical stresses along loaded diameter.

Meanwhile, it is found that the tensile stress zone in the loading BD specimen gradually decreases towards the center of the disc with the increase in the loading angle; that is, increasing the loading angle reduces the tensile stress zone in the loading direction of the disc and increases the possibility of cracking at the center. It is found that increasing the loading angle can obviously reduce the compressive stress value and stress concentration at the loading place, thus reducing the possibility of compression failure of the BD specimen near the loading and creating conditions for the specimen to take the lead in central tensile splitting failure.

According to Griffith strength criterion [38,39] to judge the damage of SCC, the specific form is:

$$\begin{cases} \sigma_G = -\frac{(\sigma_1 - \sigma_3)^2}{8(\sigma_1 + \sigma_3)} \geq \sigma_T, \sigma_1 + 3\sigma_3 \leq 0 \\ \sigma_G = |\sigma_3| \geq \sigma_T, \sigma_1 + 3\sigma_3 > 0 \end{cases} \quad (1)$$

where $\sigma_1 \geq \sigma_2 \geq \sigma_3$ are three principal stresses, which satisfy this relationship in turn.

In the loading diameter direction ($x = 0$), it can be known from Formula (1) that τ_{xy} is 0, and it is easy to judge that $\sigma_y \geq \sigma_x$ corresponds to $\sigma_1 \geq \sigma_3$. By Griffith strength criterion, $\sigma_1 + 3\sigma_3 \leq 0$, so it can be expressed as:

$$\sigma_1 + 3\sigma_3 = \frac{4P}{2\pi r H \sin(\theta/2)} \left(-\frac{b_1}{a_1} - \frac{b_3}{a_3} + 2c_1 + 2c_3 + 2\sin\theta/2\cos\theta/2 \right) \quad (2)$$

$$f_1 = (\sigma_1 + 3\sigma_3) / (P/2\pi r H) \quad (3)$$

After dimensionless $\sigma_1 + 3\sigma_3$ is recorded as f_1 , it can be seen from Figure 8 that the loading angle satisfies $\sigma_1 + 3\sigma_3 \leq 0$ from 20° to 30°. Combining Formula (4) with (1) and (2), it can be further obtained that the Griffith equivalent stress on the loading diameter of the loading BD specimen is:

$$\sigma_G = \frac{-P(b_1/a_1 + b_3/a_3)^2}{4\pi r H \sin(\theta/2)(c_1 + c_3 + \sin\theta/2\cos\theta/2)} \quad (4)$$

$$f_2 = \sigma_G / (P/2\pi r H) \quad (5)$$

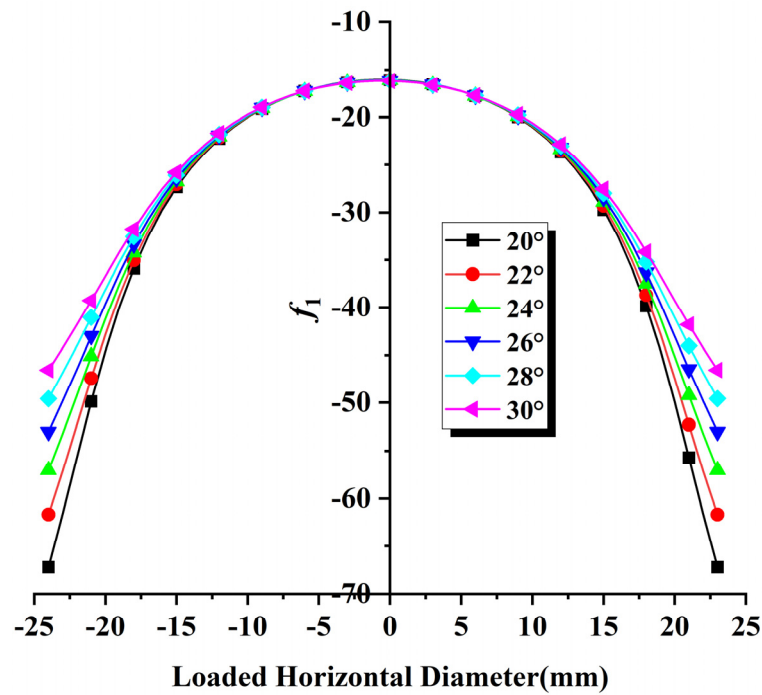


Figure 8. Non-dimensional Griffith decision conditions along loaded diameter.

After dimensionless Griffith’s equivalent stress is recorded as f_2 , the relationship between its value and loading angle is as shown in Figure 9.

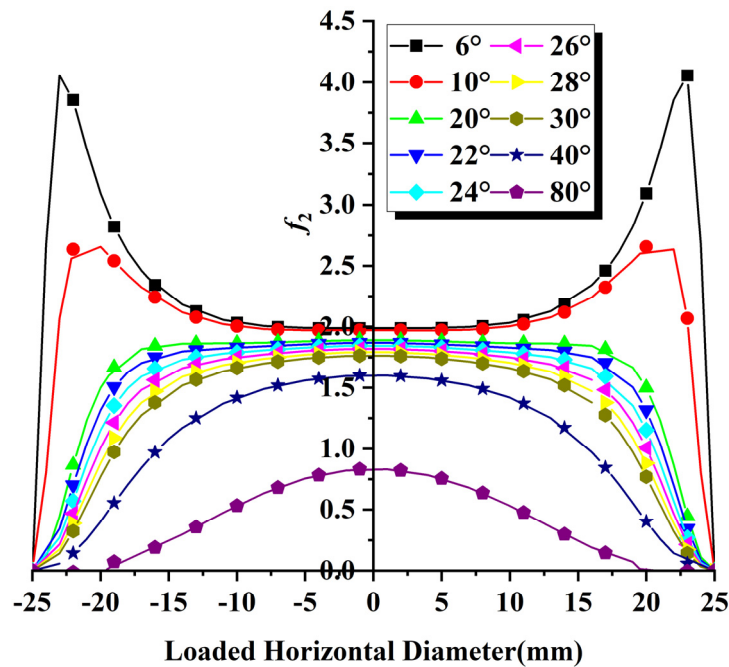


Figure 9. Non-dimensional Griffith equivalent stresses along loaded diameter.

When the loading angle is less than 20° , f_2 increases first and then decreases from the disc O to A_1 and A_2 , as shown in Figure 9. It indicates that Griffith equivalent stress at the loading end of BD is larger than that at the center O . It cannot meet the crack initiation requirement at the center and be used to measure the tensile strength of SCC.

When the loading angle is between 20° and 30° , f_2 decreases from disc O to A_1 and A_2 , from 1.88 when the loading angle is 20° to 1.77 when the loading angle is 30° , and its change rate with the loading angle is 0.11. At the same time, it is found that f_2 gradually decreases to the center of the disc with the increase in the loading angle, and the Griffith equivalent stress zone approaches to the center of the specimen, which makes it easier for the specimen to start from the middle. When the loading angle is greater than 30° , the value of f_2 decreases rapidly at the disc O, and its tensile stress is not enough to destroy the center point of the specimen.

4. Experimental Procedures

4.1. Specimen Preparation

To investigate the optimal loading angle in the flattened BD test for SCC, this paper manufactured the molds with the loading angles [40,41] θ of 20° , 22° , 24° , 26° , 28° , and 30° by a 3D printer with the material of high-strength resin. The height of the model is 25 mm, the inner diameter is 50 mm, and the outer diameter is 60 mm, as shown in Figure 10. The printing accuracy is 0.01 mm, which could meet the requirements of flatness and parallelism of the loading surfaces.

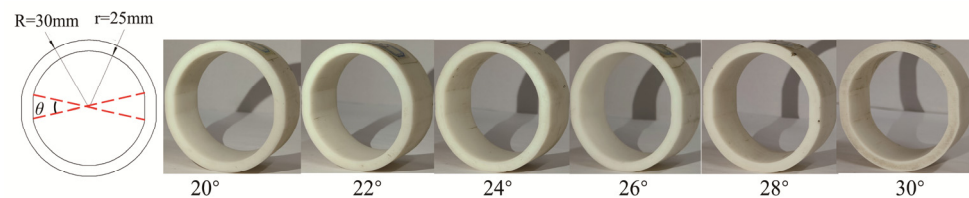


Figure 10. Mold sketch and 3D-printed molds.

According to the ratio in Table 3, the concrete specimen was mixed into a uniform slurry state and poured into the molds. The specimens were demolded one day after pouring and solidified for 28 days in a stable environment with a temperature of $(20 \pm 2)^\circ\text{C}$ and humidity of 95%.

Table 3. The mix of self-compacting concrete (kg/m^3).

Cement	Fly Ash	Water	Grit	Admixture
495	48	160	830	14

A layer of white paint was sprayed on the front face of the specimen with black speckles spotted for DIC algorithm. Five strain gauges, numbered 1#, 2#, 3#, 4#, and 5#, were equally attached to the opposite face of the specimen along the loading diameter direction, which assisted to monitor the cracking development (Figure 11). The basic physical and mechanical properties of SCC are list in Table 4.

Table 4. Basic physical and mechanical properties of concrete.

Specimen	Density/ $(\text{g}\cdot\text{cm}^{-3})$	Peak Stress/MPa	Peak Strain	Elastic Modulus/MPa	Deformation Modulus/GPa	Poisson's Ratio
SCC	2.425	52	0.0213	4.981	1.732	0.25

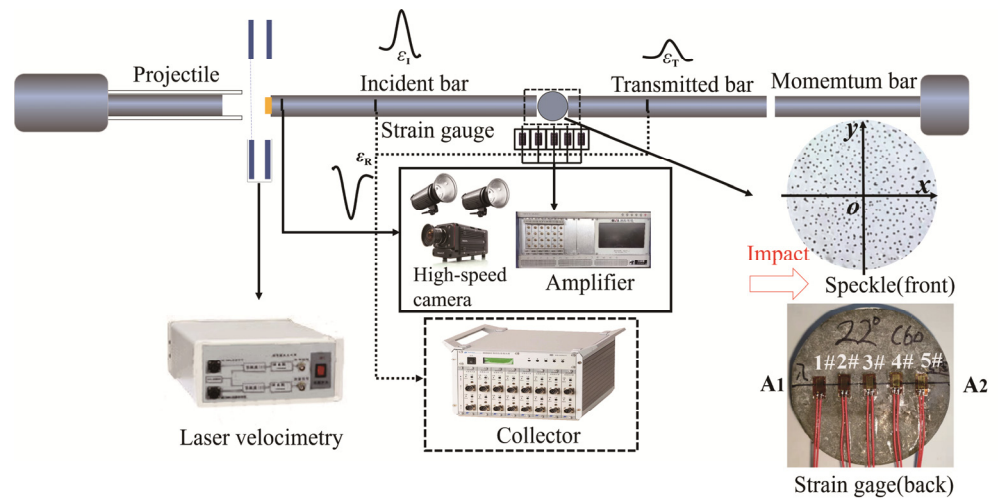


Figure 11. Schematic of the testing system.

4.2. Experimental Apparatus

The schematic of the testing system is shown in Figure 11. The SHPB is made of high-strength steel with a diameter of 75 mm, elastic modulus of 195 GPa, and yield strength of 1.10 GPa. The image acquisition system is composed of an ultra-high-speed camera, lighting system, trigger, and synchronous control system. The frame rate and exposure time of ultra-high-speed camera IDT Y7S3 were configured at 100,000 fps and 100 ns, respectively. The strain field of the specimen was extracted using DIC in which the subset size was of 31 pixels and the step size was of 5 pixels.

4.3. Loading Procedure

Each loading angle is carried out under three impact pressures, namely, 0.12 MPa, 0.20 MPa, and 0.30 MPa to achieve different loading rates. The specific test protocol is shown in Table 5. A typical raw strain pulse recorded by strain gauges attached on bars and the force balance curve at both ends of the specimen are shown in Figure 12. The three-wave method [31] was adopted to calculate the dynamic tensile strength of the flattened BD specimen as follows:

$$\sigma_T = k \frac{P}{\pi r H} = k \frac{E_0 D_0^2}{8rH} (\epsilon_I + \epsilon_R + \epsilon_T) \quad (6)$$

where k is a function of θ calculated by finite element by Griffith criterion [23]. The values of k are 0.963, 0.956, 0.948, 0.940, 0.931, and 0.921 corresponding to $\theta = 20^\circ, 22^\circ, 24^\circ, 26^\circ, 28^\circ,$ and 30° , respectively. According to the strain signal, the loading rate of tensile stress of the concrete specimen is obtained from the slope of a quasi-linear section in tensile stress history (Figure 13).

Table 5. Testing speed and loading rate.

Test Number	P/MPa	v/m·s ⁻¹	\bar{v}	$\dot{\sigma}$ /GPa·s ⁻¹	$\bar{\dot{\sigma}}$
1	0.12	4.7	4.9	364	343
	0.12	5.1		328	
	0.12	4.9		338	
2	0.20	9.8	9.6	583	587
	0.20	9.7		540	
	0.20	9.3		667	
3	0.30	12.3	12.5	790	764
	0.30	12.5		742	
	0.30	12.8		761	

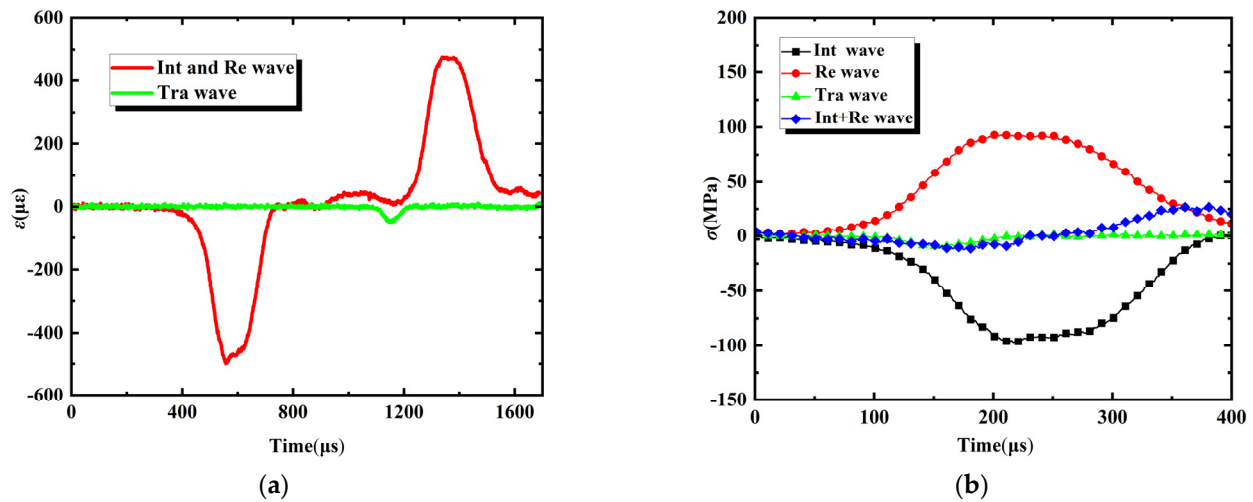


Figure 12. Waveforms and dynamic stress equilibriums of specimens in a typical flattened BD test (impact speed: 5.1 m/s). (a) Raw strain signals obtained from the strain gauges attached on the bars. (b) Dynamic force balance at both ends of the specimen.

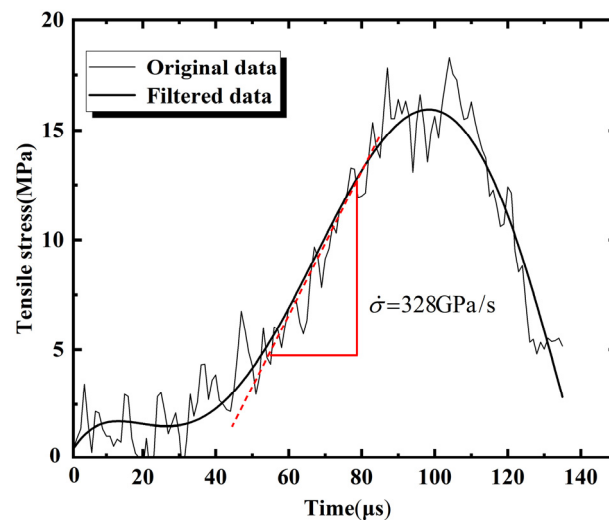


Figure 13. Calculation of the loading rate.

5. Results and Analysis

5.1. Crack Development in Flattened BD Test

Figure 14 illustrates the evolution of the strain field of the flattened BD specimen in the y direction during the dynamic loading extracted by DIC. By analyzing the splitting process of dynamic loadings of SCC, it is found that the prefabricated loading angle in the specimen has an obvious influence on the splitting process of SCC under dynamic load.

When the loading angle is in the range of $0^\circ \sim 24^\circ$, as shown in Figure 14a–d, the BD specimen starts to fracture at the loading point and expands from the other end along the loading direction. It does not meet the center cracking assumption required by the BD experiment [42], which was consistent with the results of the numerical simulations above for the conventional Brazilian disc analysis. Therefore, the loading angle θ in the range of $20^\circ \sim 24^\circ$ is not enough to effectively reduce the stress concentration at the end under the action of dynamic load.

When the loading angle is 26° , as shown in Figure 14e, the crack propagation of the specimen becomes independent from the impact speed. This loading angle can be regarded as a critical value representing the transition from non-center initiation to center initiation.

When the loading angle is in the range of $28^\circ \sim 30^\circ$ (Figure 14f,g), despite the increase in impact speed, the concentrated zone of tensile strain begins to appear in the center of the flattened BD specimen and then expands to both ends, which satisfies the validity condition of the BD dynamic tensile test. The BD specimen O first reaches the critical tensile strain value when the concrete is damaged, breaks and quickly expands to a crack parallel to the loading direction towards both ends of the specimen.

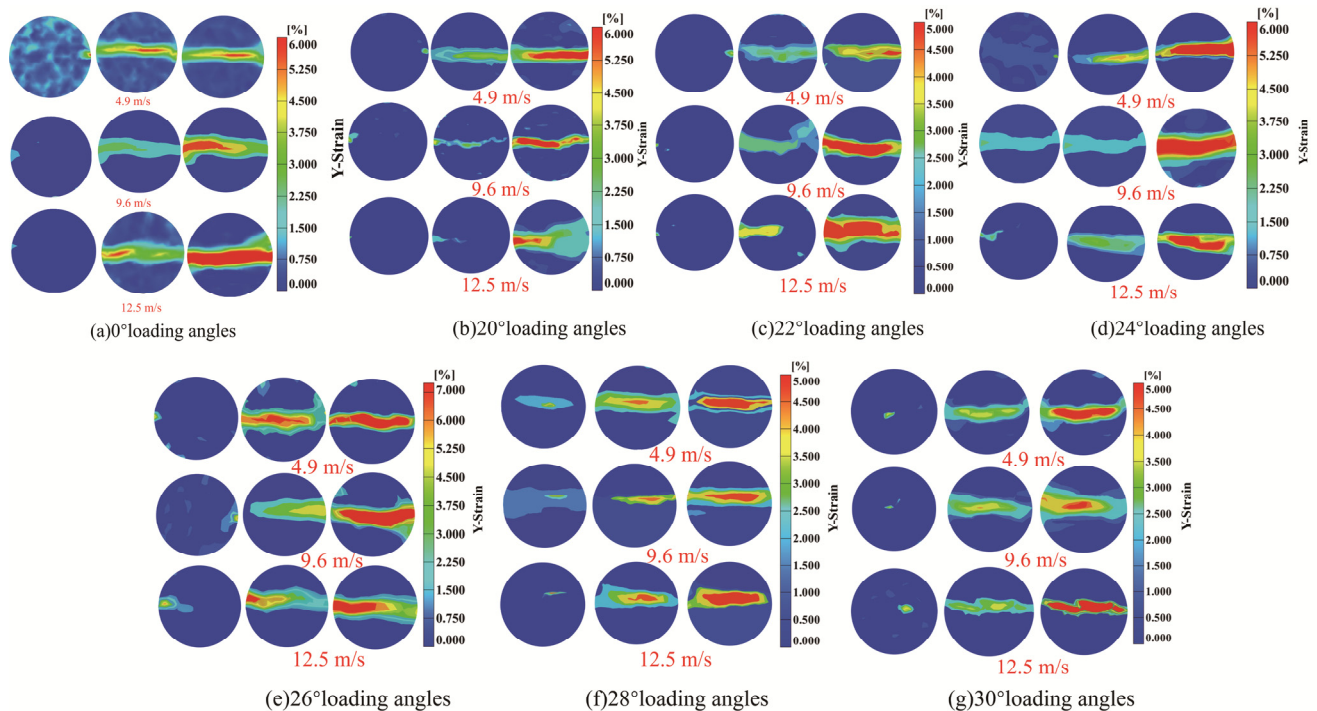


Figure 14. Vertical strain field of BD specimen at different loading angles and impact velocities.

5.2. Strain Analysis of Crack Propagation in BD Specimen

To confirm the results obtained by DIC, the location and sequence of crack initiation were also examined from the strains recorded by strain gauges at different locations of the disc specimen under different loading angles, as shown in Figure 15. As can be seen from Figure 15, the maximum principal strain at the monitoring point under impact loading first exhibits a nonlinear variation, indicating an increasing degree of damage at this point. Fracture occurs when the damage at this point reaches its maximum level. The sudden increase in strain at the monitoring point is defined as the failing moment for each strain gauge. Due to the dense data, it is not appropriate to discern from the graph, but the strain value of the mutation point can be accurately identified in the raw data text. Since the sampling frequency of the dynamic acquisition instrument is set to 2 MHz, the strain value corresponding to each time can be seen in the raw data text. By importing the data into origin in the form of a picture that cannot be easily discriminated, the mutation point can be easily identified through the raw data text. Hence, the point where the sudden change in strain occurs in the experiment is taken as the fracture point of the specimen, and the failure strain at this time is reliable from the data of previous studies. It can be seen that the average failure strain is 6.61×10^{-3} at an impact velocity of 9.6 m/s and a loading angle of 20° .

Under the action of the average impact speed of 4.9 m/s, when the loading angle is less than 26° , the time of fracture of the 5# strain gauge is earlier than that of the 1# strain gauge, and the response to the force wave action is the first; the overall trend at the moment of fracture of the strain gauge is left high and right low as shown in Figure 16a, indicating that the crack propagation starts from the A_2 end; with the increase in the impact speed,

the moment of fracture of the strain gauge changes, and the overall trend is left low and right high (Figure 16b,c), indicating that the crack propagation starts from the A1 end. The validity and correctness of DIC and numerical simulation are further verified. When the loading angle is greater than 26° , the moment of fracture of the SCC is not affected by the impact speed, and it occurs in the middle of the specimen.

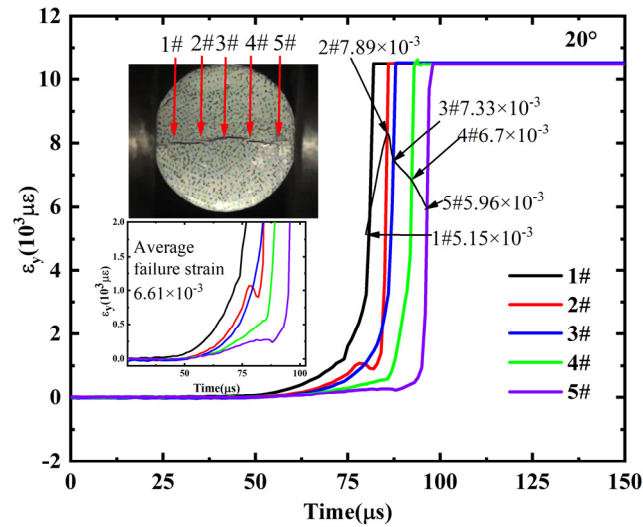


Figure 15. Strain history of the crack opening.

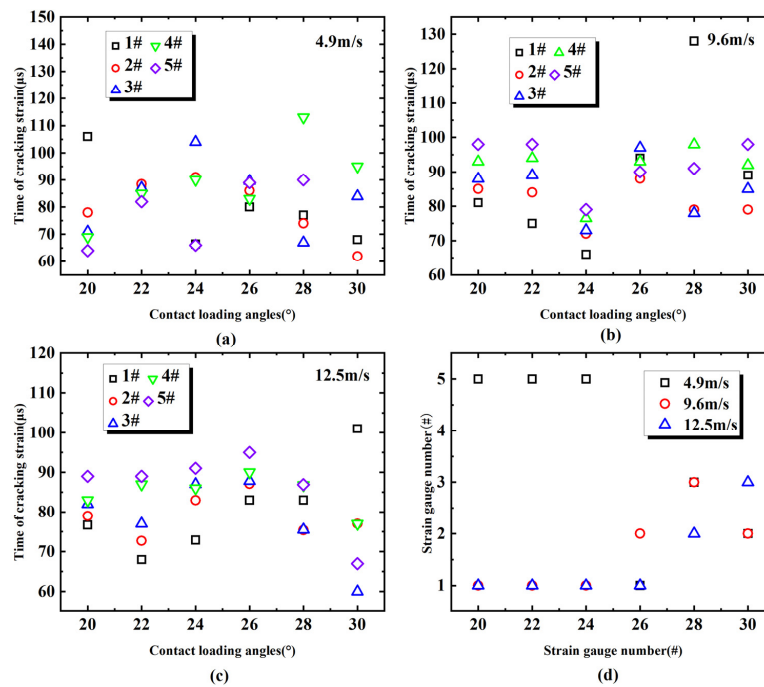


Figure 16. (a) Crack extension time sequence at 4.9 m/s; (b) Crack extension time sequence at 9.6 m/s; (c) Crack extension time sequence at 12.5 m/s; (d) Start cracking point sequence.

It is clear from Figure 16d that as the loading angle increases, the first crack point of the crack moves closer to the middle of the specimen. The time of crack propagation in the BD is directly related to the impact velocity, and the overall performance is that the time for the crack to expand in the BD is shortened with the increase in speed. When the cracking point is amalgamation, the crack propagation time is $53 \mu\text{s}$ at a velocity of 4.9 m/s. At a speed of 9.6 m/s, the crack propagation time is $32 \mu\text{s}$, and the time is reduced to 39.6%. When the

crack is cracked in the center, the crack propagation time is relatively shortened, expanding from the center point to both sides, and the expansion time is basically maintained at 20 μs. The crack propagation time is about half as short as that of non-intermediate initiation.

The test and theoretical analysis get consistent results, corroborate each other’s correctness and further reduce the size of the platform loading angle, improve the accuracy of the test, and better serve similar materials such as concrete. At the platform angle less than 20°, there is an obvious stress concentration phenomenon at the loading end, which cannot meet the central cracking requirement, and a clear explanation can be given by both numerical mode and theory.

If the platform angle is located between 20°~26°, although the disc center point O stress reached the maximum (even though near the loading ends of the stress is still relatively large), at the same time, the loading end of the disc is affected by the composite effect of tension and compression, so the central stress is still insufficient to make the specimen from the center point O first crack. When the platform angle is increased to 28°~30°, the stress at the center point O reaches the maximum, while the stress at the loading end is significantly reduced, eliminating the phenomenon of stress concentration at the end, which well explains the rationality of this platform angle loading and provides a clear direction for the subsequent development of other material tests. By further increasing the platform angle, although the stress at the center point is the largest, its value is not large enough to cause the specimen to fracture.

5.3. Influence of Loading Angle on Tensile Strength of Specimens

The relationship between dynamic tensile strength and average loading rate of BD specimens on six loading angles is demonstrated in Figure 17. With the increase in loading rate, the dynamic tensile strength of BD specimens shows an increasing trend. When the loading rate is at relatively the same range, the larger the loading angle is, the greater the dynamic tensile strength of the BD specimen is. For loading angles less than 28°, the tensile strength decreases successively. The reason is relevant to the first crack position of the crack. When the crack firstly develops at the end of the specimen, the shear failure occurs at the edge and cause less tensile resistance being effective. Therefore, the tensile strength measured at a loading angle less than 28° underestimates the inherent tensile strength.

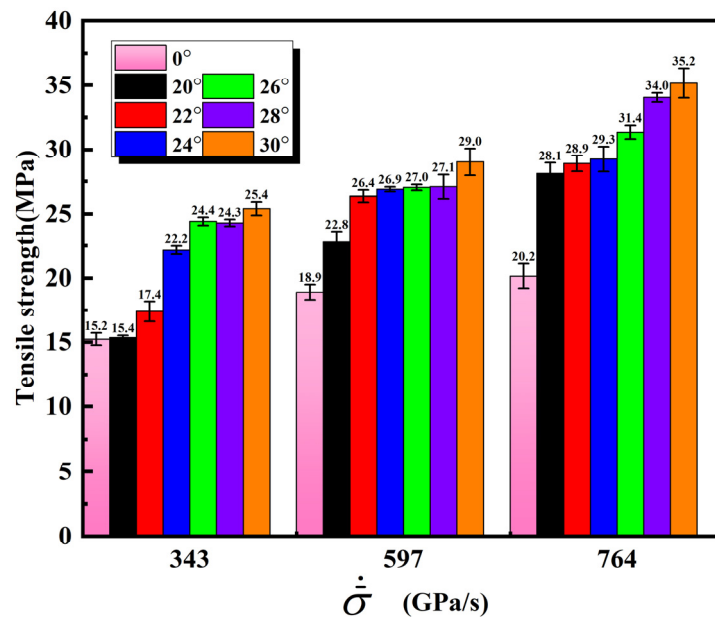


Figure 17. Relationship between dynamic tensile strength and loading rate.

6. Conclusions

Based on the numerical simulation and theoretical analysis, the influence of the introduction of the platform loading angle on the stress field of the Brazilian disc is obtained. Under the known relationship between the platform angle and the stress field, the Brazilian disc test under the dynamic splitting platform is designed to obtain the platform Angle range suitable for concrete and other similar materials. The following conclusions can be obtained through comprehensive analysis:

- (1) The numerical simulation results show that the starting point of the traditional Brazilian disc is affected by the loading speed. When the loading speed is relatively small, the crack propagation direction is from the transmission bar end to the incident bar end. When the loading speed is increased, the crack growth direction is changed. It is essentially related to stress wave propagation.
- (2) The Griffith equivalent stress theory well explained the optimal loading angle range in flattened BD tests on concrete from a theoretical view. With the increase in the loading angle, the maximum stress transferred from the loading end to the center of the specimen.
- (3) The optimal loading angle in dynamic flattened Brazilian disc splitting test for concrete is between 28° and 30° . For different loading rates, this loading angle can still effectively ensure the central cracking of the specimen.
- (4) At the same loading rate, the dynamic tensile strength with non-center crack initiation obtained from the loading angle less than 28° underestimates the inherent tensile strength.

7. Further Research

Further research may include the following:

- (1) Carrying out the effect of loading angle on crack extension for different strength concretes.
- (2) Carrying out the crack evolution process in 3D space on the basis of experiments with the help of numerical simulations.
- (3) Performing simulations to explore the crack extension mechanism of other similar materials.

Author Contributions: Conceptualization, C.M., J.L., and H.X.; methodology, B.S.; software, B.S. and C.M.; validation, C.M. and B.S.; formal analysis, B.S.; investigation, W.L. and T.X.; resources, B.S.; data curation, B.S.; writing—original draft preparation, B.S.; writing—review and editing, B.S. and H.X.; visualization, H.X.; supervision, C.M.; project administration, B.S.; funding acquisition, H.X. All authors have read and agreed to the published version of the manuscript.

Funding: This work was financially supported by the Natural Science Foundation of Jiangsu Province (BK20200583, BK20221528) and Anhui Province (2108085QA40) and the National Natural Foundation of China (12072371, 52279120).

Institutional Review Board Statement: Not applicable.

Informed Consent Statement: Not applicable.

Data Availability Statement: The data used to support the findings of this study are available from the corresponding author upon request.

Conflicts of Interest: The authors declare no conflict of interest.

Nomenclature

a_1, a_2, a_3, a_4	Intermediate variable	N	Pressure hardening exponent
A	Normalized cohesive strength	μ_c, μ_l	Crushing volumetric strain, Locking volumetric strain
A_1, A_2	Incident bar, transmission bar and disc contact surface, respectively	P_C, P_1, P	Crushing pressure, Locking pressure, peak load
b_1, b_2, b_3, b_4	Intermediate variable	ρ	Mass density
B	Normalized pressure hardening	$\epsilon_I, \epsilon_T, \epsilon_R$	Strain signals of the incident, reflected and transmitted waves
c_1, c_2, c_3, c_4	Intermediate variable	$\sigma_x, \sigma_y, \tau_{xy}, \sigma_G, \sigma_T$	Horizontal stress, vertical stress, shear stress, Griffith's equivalent stress and the tensile strength of concrete of the point
D_0, D_1, D_2	Damage constant	$\sigma_{xmax}, \sigma_{ymax}, \sigma_{x1max}$	x,y-compressive stress, x-tensile stress
E_0	Elasticity modulus	θ	Loading angle
ϵ_{fmin}	Amount of plastic strain before fracture	f_1, f_2	Dimensionless stress, dimensionless Griffith's equivalent stress
f_C	Compressive strength	K_1, K_2, K_3	Pressure constant
G	Shear modulus	H, R, r	Height and outer radius and the inner radius
T	Maximum tensile hydrostatic pressure	$\sigma_1, \sigma_2, \sigma_3$	Three principal stresses
v, \bar{v}	Impact velocities	$\dot{\sigma}, \bar{\sigma}$	Loading rate

Appendix A

$$\begin{cases} \sigma_x = \frac{P}{2\pi r H \sin \frac{\theta}{2}} \left(\frac{b_1}{a_1} + c_1 + \frac{b_2}{a_2} - c_2 + \frac{b_3}{a_3} + c_3 + \frac{b_4}{a_4} - c_4 \right) + \frac{P \cos \frac{\theta}{2}}{\pi r H} \\ \sigma_y = \frac{-P}{2\pi r H \sin \frac{\theta}{2}} \left(\frac{b_1}{a_1} - c_1 + \frac{b_2}{a_2} + c_2 + \frac{b_3}{a_3} - c_3 + \frac{b_4}{a_4} + c_4 \right) + \frac{P \cos \frac{\theta}{2}}{\pi r H}, \\ \tau_{xy} = \frac{P}{2\pi r H \sin \frac{\theta}{2}} \left[\frac{(r \cos \frac{\theta}{2} + x)^2}{a_1} - \frac{(r \cos \frac{\theta}{2} + x)^2}{a_2} - \frac{(r \cos \frac{\theta}{2} - x)^2}{a_3} + \frac{(r \cos \frac{\theta}{2} - x)^2}{a_4} \right] \end{cases} \quad (A1)$$

Among:

$$\begin{cases} a_1 = (r \cos \frac{\theta}{2} + x)^2 + (y - r \sin \frac{\theta}{2})^2, a_2 = (r \cos \frac{\theta}{2} + x)^2 + (y + r \sin \frac{\theta}{2})^2 \\ a_3 = (r \cos \frac{\theta}{2} - x)^2 + (y - r \sin \frac{\theta}{2})^2, a_4 = (r \cos \frac{\theta}{2} - x)^2 + (y + r \sin \frac{\theta}{2})^2 \\ b_1 = (r \cos \frac{\theta}{2} + x)(r \sin \frac{\theta}{2} - y), b_2 = (r \cos \frac{\theta}{2} + x)(r \sin \frac{\theta}{2} + y) \\ c_1 = \arctan \left(\frac{y - r \sin \frac{\theta}{2}}{r \cos \frac{\theta}{2} + x} \right), c_2 = \arctan \left(\frac{y + r \sin \frac{\theta}{2}}{r \cos \frac{\theta}{2} + x} \right) \\ b_3 = (r \cos \frac{\theta}{2} - x)(r \sin \frac{\theta}{2} - y), b_4 = (r \cos \frac{\theta}{2} - x)(r \sin \frac{\theta}{2} + y) \\ c_3 = \arctan \left(\frac{y - r \sin \frac{\theta}{2}}{r \cos \frac{\theta}{2} - x} \right), c_4 = \arctan \left(\frac{y + r \sin \frac{\theta}{2}}{r \cos \frac{\theta}{2} - x} \right) \end{cases} \quad (A2)$$

References

1. Healy, D.; Jones, R.R.; Holdsworth, R.E. Three-dimensional brittle shear fracturing by tensile crack interaction. *Nature* **2006**, *439*, 64–67. [CrossRef] [PubMed]
2. Song, W.; Zhao, W.; Tan, X. An Experimental Study on Dynamic Mechanical Properties of Fiber-Reinforced Concrete under Different Strain Rates. *Appl. Sci.* **2018**, *10*, 1904.
3. Temsah, Y.; Jahami, A.; Khatib, J.; Sonebi, M. Numerical analysis of a reinforced concrete beam under blast loading. In Proceedings of the MATEC Web Of Conferences, Rabat, Morocco, 22–25 November 2017; Volume, 149, p. 02063. [CrossRef]
4. Temsah, Y.; Jahami, A.; Aouad, C. Silos structural response to blast loading. *Eng. Struct.* **2021**, *243*, 112671. [CrossRef]
5. Guo, Y.; Gao, G.; Jing, L.; Shim, V.P.W. Dynamic Properties of Mortar in High-strength Concrete. *Int. J. Impact Eng.* **2022**, *165*, 1–30. [CrossRef]
6. Cusatis, G. Strain-rate effects on concrete behavior. *Int. J. Impact Eng.* **2011**, *38*, 162–170. [CrossRef]

7. Zhang, Q.; Zhao, J. Determination of mechanical properties and full-field strain measurements of rock material under dynamic loads. *Int. J. Rock Mech. Min. Sci.* **2013**, *60*, 423–439. [\[CrossRef\]](#)
8. Yue, C.; Ma, H.; Yu, H.; Zhang, J.; Chen, L.; Mei, Q.; Tan, Y.; Liu, T. Experimental and Three-dimensional Mesoscopic Simulation Study on Coral Aggregate Seawater Concrete with Dynamic Direct Tensile Technology. *Int. J. Impact Eng.* **2021**, *150*, 103776. [\[CrossRef\]](#)
9. Sarfarazi, V.; Ghazvinian, A.; Schubert, W.; Nejati, H. A new approach for measurement of tensile strength of concrete. *Period. Polytech. Civ. Eng.* **2016**, *60*, 8328. [\[CrossRef\]](#)
10. Truong, V.; Kim, D. A review paper on direct tensile behavior and test methods of textile reinforced cementitious composites. *Compos. Struct.* **2021**, *263*, 113661. [\[CrossRef\]](#)
11. Songtao, L.; Liu, C.; Yao, H.; Zheng, J. Comparisons of synchronous measurement methods on various moduli of asphalt mixtures. *Constr. Build. Mater.* **2018**, *158*, 1035–1045.
12. Li, Q.; Zhang, Z.; Sang, L. Virtual experimental study on the effect of coarse aggregate angularity on tensile performance of asphalt mixtures. *J. Rail Way Sci. Eng.* **2020**, *17*, 1429–1435.
13. Wang, L.; Jia, S.; Yi, Y. Effects of damage evolution on tensile strength measurement of nuclear graphite material by ring compression test. *J. Nucl. Mater.* **2021**, *555*, 153128. [\[CrossRef\]](#)
14. Rohr, N.; Fischer, J. Effect of aging and curing mode on the compressive and indirect tensile strength of resin composite cements. *Head Face Med.* **2017**, *13*, 22. [\[CrossRef\]](#) [\[PubMed\]](#)
15. Allen, R.C.; Thompson, N.; Tedesco, J.W. Split-Hopkinson Pressure-Bar tests on Concrete and Mortar in Tension and Compression. *Mater. J.* **1989**, *86*, 475–481.
16. Khosravani, M.; Silani, M.; Weinberg, K. Fracture studies of Ultra-High Performance Concrete using dynamic Brazilian tests. *Theor. Appl. Fract. Mech.* **2018**, *93*, 302–310. [\[CrossRef\]](#)
17. Shi, K.; Zhang, S. Ring Method Test on the early-Age Anti-Cracking Capability of High-Performance Lithium Slag Concrete. *Appl. Mech. Mater.* **2011**, *94–96*, 782–785.
18. Wang, C.; Gao, G.; Jia, Q. Investigation of optimum sample shape for the Luong core tension test. *Projectilin of Engineering Geology and the Environment. Engineering* **2020**, *79*, 831–844.
19. ISRM. Suggested methods for determining tensile strength of rock materials. *Int. J. Rock Mech. Min. Sci. Geomech. Abstr.* **1978**, *15*, 99–103. [\[CrossRef\]](#)
20. ISO 6508-1:2015; Metallic Materials—Rockwell Hardness Test—Part 1: Test Methods. International Organization Standardization (ISO): Geneva, Switzerland, 2015.
21. ASTM-C496; Standard Test Method for Splitting Tensile Strength of Cylindrical Concrete Specimens; Annual Book of ASTM Standards. ASTM: West Conshohocken, PA, USA, 2004; Volume 11, pp. 336–341.
22. DIN EN 12390-6; Testing Hardened Concrete—Part 6: Tensile Splitting Strength of Test Specimens. Deutsches Institut Für Normung (DIN): Berlin, Germany, 2010.
23. Liu, K.; Tanimura, S. Numerical analysis for dynamic stress concentration in a rectangular block due to impact. *Int. J. Impact Eng.* **1997**, *19*, 653–666. [\[CrossRef\]](#)
24. Ye, J.; Wu, F.; Sun, J. Estimation of the tensile elastic modulus using Brazilian disc by applying diametrically opposed concentrated loads. *Int. J. Rock Mech. Min. Sci.* **2009**, *46*, 568–576.
25. Satoh, Y. Position and load of failure in Brazilian test; A numerical analysis by Griffith criterion. *J. Soc. Mater. Sci.* **1987**, *36*, 1219–1224. [\[CrossRef\]](#)
26. Mahanta, B.; Sirdesai, N.; Sirdesai, T.N.; Ranjith, P.G. Experimental Study of Strain Rate Sensitivity to Fracture Toughness of Rock using Flattened Brazilian Disc. *Procedia Eng.* **2017**, *191*, 256–262. [\[CrossRef\]](#)
27. Hondros, G. The evaluation of Poisson's ratio and the modulus of materials of low tensile resistance by the Brazilian (Indirect tensile) test with particular reference to concrete. *J. Appl. Sci.* **1959**, *10*, 243–268.
28. Mellor, M.; Hawkes, I. Measurement of tensile strength by diametral compression of discs and annuli. *Eng. Geol.* **1971**, *3*, 173–225. [\[CrossRef\]](#)
29. Markides, C.F.; Papis, D.N.; Kourkoulis, S.K. Closed full-field solutions for stresses and displacements in the Brazilian disk under distributed radial load. *Int. J. Rock Mech. Min. Sci.* **2010**, *47*, 227–237. [\[CrossRef\]](#)
30. Wang, Q.; Xing, L. Determination of fracture toughness KIC by using the flattened Brazilian disk specimen for rocks. *Eng. Fract. Mech.* **1999**, *64*, 193–201. [\[CrossRef\]](#)
31. Robert, P.; Marcin, K. Influence of Imperfect Position of a Striker and Input Bar on Wave Propagation in a Split Hopkinson Pressure Bar (SHPB) Setup with a Pulse-Shape Technique. *Appl. Sci.* **2020**, *10*, 2423.
32. Wang, M.; Cao, P. Numerical study on flattened Brazilian test and its empirical formula. *Electron. J. Geotech. Eng.* **2015**, *20*, 12211–12224.
33. Wang, M.; Cao, P. Numerical Analysis of Flattened Brazilian Disc Test Based on the Cusp Catastrophe Theory. *Math. Probl. Eng.* **2016**, *2016*, 4517360. [\[CrossRef\]](#)
34. Kaklis, K.; Agioutantis, Z.; Sarris, E.; Pateli, A. A theoretical and numerical study of discs with flat edges under diametral compression (flat Brazilian test). In Proceedings of the 5th GRACM International Congress on Computational Mechanics, Limassol, Cyprus, 29 June–1 July 2005; pp. 437–444.

35. Kucewicz, M.; Baranowski, P.; Malachowski, J. Dolomite fracture modeling using the Johnson-Holmquist concrete material model: Parameter determination and validation. *J. Rock Mech. Geotech. Eng.* **2021**, *13*, 335–350. [[CrossRef](#)]
36. Pajak, M.; Baranowski, P.; Janiszewski, J. Experimental testing and 3D meso-scale numerical simulations of SCC subjected to high compression strain rates. *Constr. Build. Mater.* **2021**, *302*, 124379. [[CrossRef](#)]
37. Huang, Y.; Wang, L.; Lu, Y.; Chen, J.R.; Zhang, J.H. Semi-analytical and Numerical Studies on the Flattened Brazilian Splitting Test Used for Measuring the Indirect Tensile Strength of Rocks. *Rock Mech. Rock Eng.* **2015**, *48*, 1849–1866. [[CrossRef](#)]
38. Griffith, F. The Phenomena of Rupture and Flow in Solids. *Philos. Trans. R. Soc. London. Ser. A Contain. Pap. A Math. Or Phys.* **1921**, *221*, 163–198.
39. Hoek, E.; Martin, C. Fracture initiation and propagation in intact rock—A review. *J. Rock Mech. Geotech. Eng.* **2014**, *6*, 287–300. [[CrossRef](#)]
40. Ammeri, A.; Neifar, M.; Ibrahim, K. Experimental and Numerical Study of the Split Tensile Test on a Silty Soil: Discrete Element Analysis. *IJEART* **2016**, *5*, 929–936.
41. Yu, Q.; Tang, C.; Yang, T.; Tang, S.; Liu, H. Numerical analysis of influence of central angle of flats on tensile strength of granite in split test with flattened disc. *Rock Soil Mech.* **2008**, *29*, 3251–3255+3260.
42. Bahaaddini, M.; Mehdi, S.; Hossein, M.; Rahimi, E. Numerical assessment of rupture mechanisms in Brazilian test of brittle materials. *Int. J. Solids Struct.* **2019**, *180*, 1–12. [[CrossRef](#)]